ARTICLE

Facile and General Method to Synthesize Pt-Based High-Entropy-Alloy Nanoparticles

Panchao Zhao,* Qigao Cao,* Wei Yi,* Xiaodong Hao,* Jigang Li, Bosheng Zhang, Long Huang, Yujie Huang, Yunbo Jiang, Bingshe Xu, Zhiwei Shan,* and Jialin Chen*

Read Online

ACCESS | Metrics & More | Article Recommendations | SI Supporting Information

ABSTRACT: Pt-based high-entropy-alloy nanoparticles (HEA-NPs) have excellent physical and chemical properties due to the diversity of composition, complexity of surface structure, high mixing entropy, and properties of nanoscale, and they are used in a wide range of catalytic applications such as catalytic ammoxidation, the electrolysis of water to produce hydrogen, CO_2/CO reduction, and ethanol/methanol oxidation reaction. However, offering a facile, low-cost, and large-scale method for preparing Pt-based HEA-NPs still faces great challenges. In this study, we employed a spray drying technique combined with thermal decomposition reduction (SD-TDR) method to synthesize a single-phase solid solution from binary nanoparticles to denary Pt-based HEA-NPs containing 10 dissimilar elements loaded on carbon supports in an H_2 atmosphere with a moderate heating rate (3 °C/min), thermal decomposition temperature (300−850 °C), duration time (30 min), and low cooling rate (5−10 °C/min). The Pt autocatalytic behavior was found and investigated, confirming that Pt element could decrease the reduction temperature of other metals via autocatalytic behavior. Therefore, using the feature of Pt autocatalytic behavior, we have achieved Pt-based HEA-NPs at a minimum temperature of 300 °C. We not only prepared a series of Pt-based HEA-NPs with targetable ingredient, size, and phase using the SD-TDR method but also proved the expandability of the SD-TDR technique by synthesizing Pt-based HEA-NPs loaded on different supports. Moreover, we investigated methanol oxidation reaction (MOR) on as-synthesized senary PtCoCuRuFeNi HEA-NPs, which presented superior electrocatalytic performance over commercial Pt/C catalyst.

KEYWORDS: high-entropy-alloy nanoparticles, Pt-based nanomaterials, spray drying technique, Pt autocatalytic behavior, single-phase solid solution
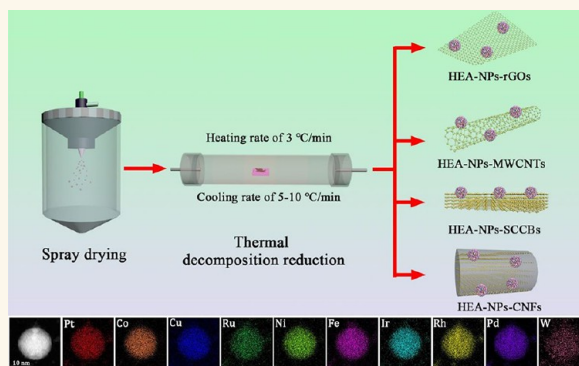
INTRODUCTION

High-entropy-alloy nanoparticles (HEA-NPs) are composed of five or more metal elements (each element mole percentage ranged from 5% to 35%) and have a single-phase solid solution structure in a single nanoparticle without phase-separated or segregation of elements.[1−14] Platinum (Pt) metal is widely used in various catalytic reactions due to its excellent catalytic performance; so, at present, numerous HEA-NPs contain Pt. Pt-based HEA-NPs are deployed in a wide range of applications such as catalytic ammoxidation,[1,2] the electrolysis of water to produce hydrogen,[3−9] CO_2/CO reduction,[10,11] and ethanol/methanol oxidation reaction,[12−14] due to their excellent physical and chemical properties caused by diversity of composition, complexity of surface structure, high mixing entropy, and properties of nanoscale.[1,2,15] However, Pt-based HEA-NPs were difficult to synthesize until the carbothermal shock (CTS) method was reported in 2018.[1] Yao et al. systematically synthesized Pt-based HEA-NPs by the CTS

method, which successfully mixed eight elements evenly in nanoparticles to form a single-phase solid solution. Nowadays, the main methods of synthesizing Pt-based HEA-NPs, including the carbothermal shock (CTS) method (temperature ~1727 °C, 55 ms duration, heating and cooling rate of ~10^5 °C/s), fast moving bed pyrolysis (FMBP) strategy (temperature ~650 °C, heating rate of ~130 °C/s), and microwave heating (MH) method (temperature ~1676 °C, rapid heating ~5 s, cooling rate of ~10^4 °C/s), are to expose precursor-impregnated carrier materials to extremely high heating and
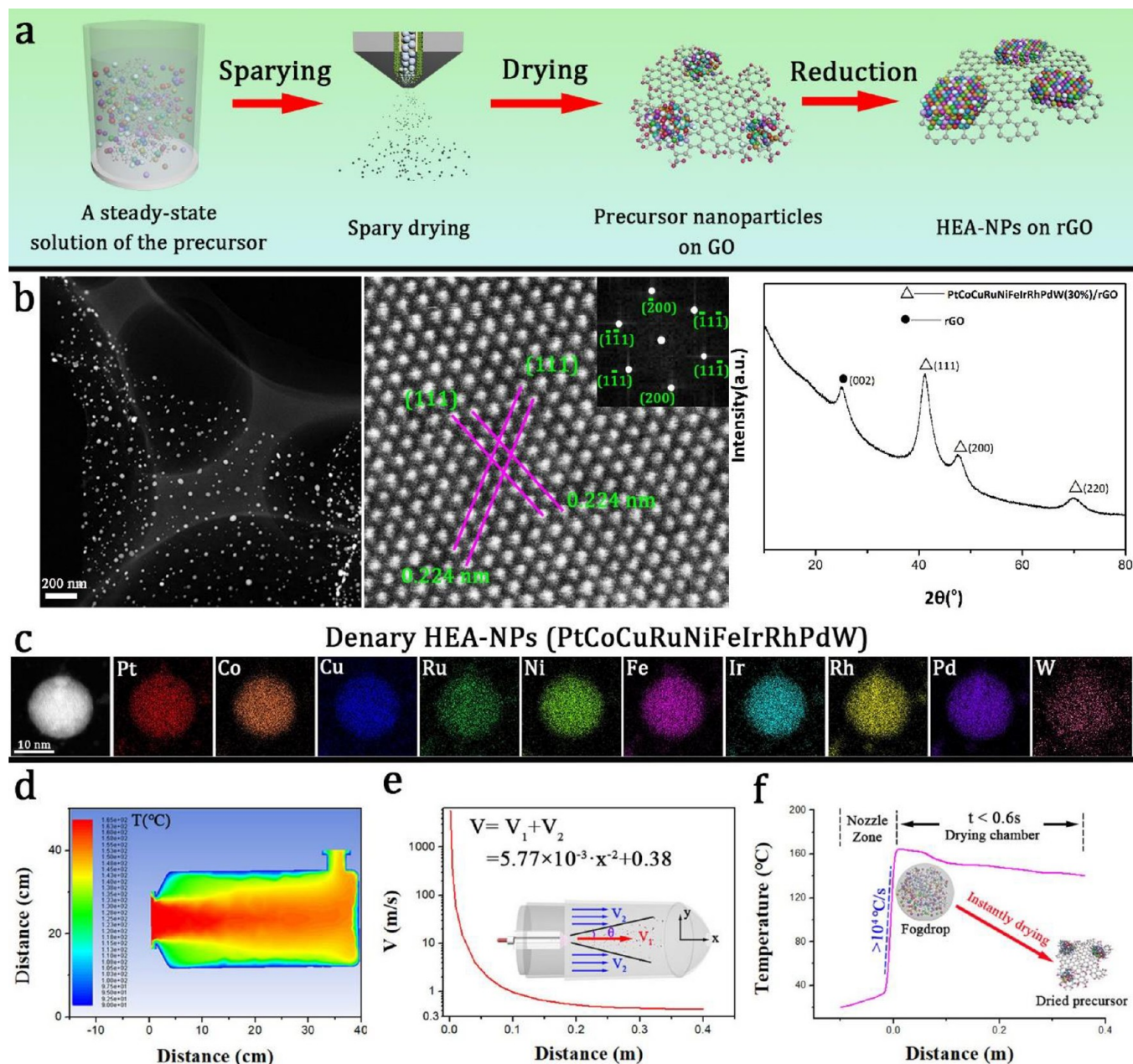
Figure 1. SD-TDR synthesis of HEA-NPs loaded onto rGO. (a) Description scheme of synthetic process of HEA-NPs: The pretreated steady-state solution of precursors and GO mixed evenly was spray-dried to form multimetallic precursor nanoparticles on GO. After thermal decomposition reduction, the HEA-NPs loaded on rGO were obtained. (b) HAADF-STEM images and XRD pattern for denary PtCoCuRhFeIrRuNiPdW HEA-NPs. The inset is the corresponding FFT pattern. (c) STEM-EDS elemental maps of denary HEA-NPs with 10 dissimilar elements (Pt, Co, Cu, Rh, Fe, Ir, Ru, Ni, Pd, and W) obtained at a reduction temperature of 850 °C. (d) Temperature field of drying chamber. (e) Velocity of fogdrops in the center of the drying chamber. (f) Temperature curve in the center of the drying chamber.

cooling rates for breaking the restriction of metal thermodynamic immiscibility, which has been proven to be successful in preparing a series of Pt-based HEA-NPs.[1−3,16] However, those methods required rapid heating and cooling rates, complex heating equipment, good conductivity substrates (CTS), excellent heat conduction carriers (FMBP), or good microwave absorption capability (MH); as a consequence, they lead to difficulty for facile, low-cost, and large-scale synthesis of Pt-based HEA-NPs. In addition, the polyol method and dealloying method were also reported for the synthesis of Pt-based HEA-NPs. Although several HEA-NPs (PtPdRhRuIr, PtPdRhRuIrOs) were successfully synthesized by the polyol

method, it is hard to alloy more than three elements to form HEA-NPs because of the tremendous differences in reaction thermal dynamics of various metal precursors and element-specific nucleation.[17−21] And, the dealloying process is very complex and has high energy consumption. How to effectively remove the Al solvent with fixed components using lye is a big challenge, and the final products are not nanoparticles but micron particles with a the nano structure using dealloying method.[6−9] Therefore, offering a facile, low-cost and large-scale method for preparing Pt-based HEA-NPs is significant.

Here, we developed a spray drying technique combined with the thermal decomposition reduction (SD-TDR) method to
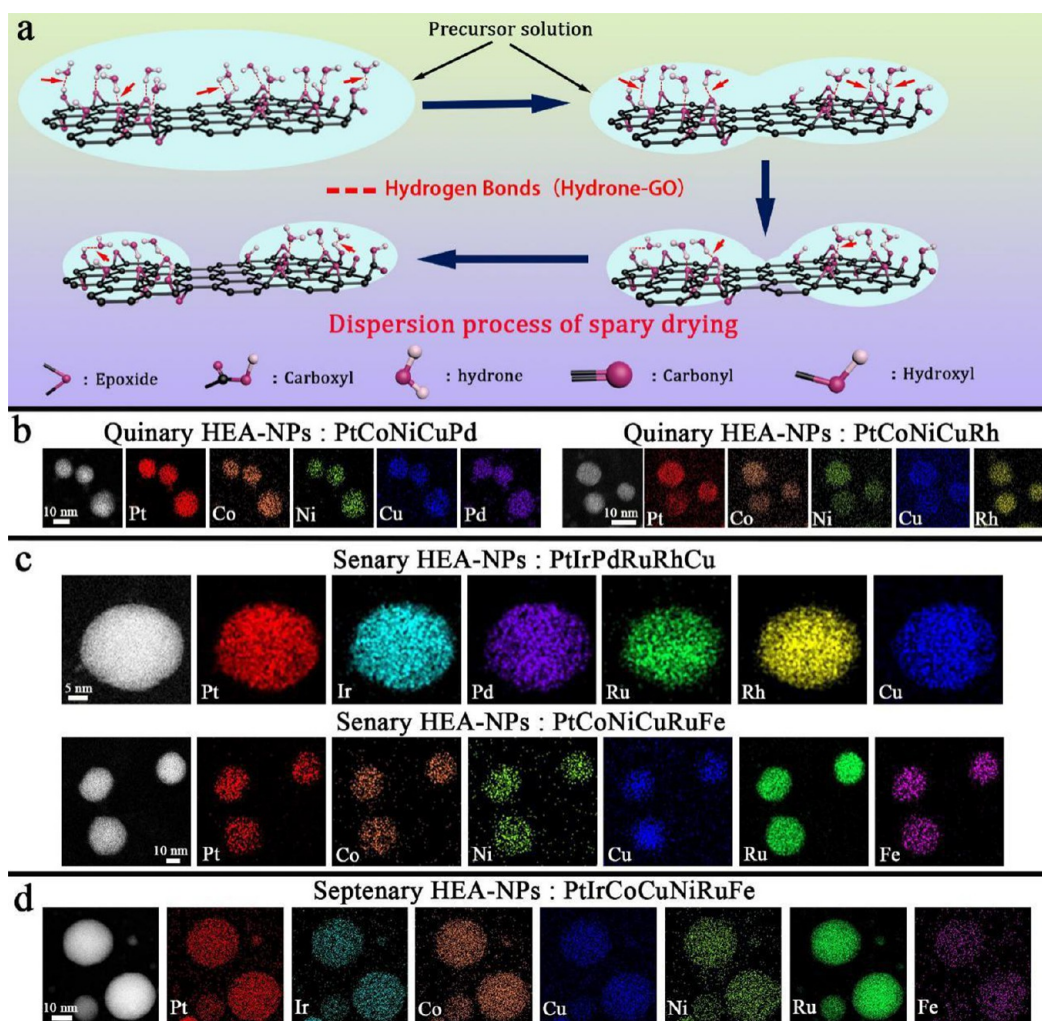
Figure 2. Dispersion process of nanoparticles and element distribution characterization of HEA-NPs, HAADF-STEM images, and STEM elemental maps. (a) Dispersion process of nanopaticles in detail: Precursor solution on the surface of GO tended to anchor where there were oxygen-containing groups to precipitate precursor nanoparticles under the guidance of an interaction force (the hydrogen bonds) between precursor solution and oxygen-containing groups. (b) Quinary (PtCoCuRuPd, PtCoCuRuRh) HEA-NPs. (c) Senary (PtIrPdRuRhCu, PtCoNiCuRuFe) HEA-NPs. (d) Septenary PtIrCoCuNiRuFe HEA-NPs. All nanoparticles were synthesized at a reduction temperature of 850 °C.

prepare Pt-based HEA-NPs containing up to 10 dissimilar metallic elements with different atom features (see details in the Supporting Information, Table S1) and element miscibility (Table S2) loaded on carbon supports. Generally, the spray drying (SD) method can be applied in electronics, catalysts, drug carriers, sensors, pigments, magnetic and optical materials, which was developed to be a rapid, low-cost, precise-controlled, and scalable technique for synthesis of nanoscale materials (See detail in Supporting Information, Figure S1).[22−27] In this work, appropriated precursors salts were dissolved in deionized water (Figure S2) and mixed with grapheme oxide (GO) (Figures S3−S4) to obtain the steady-state solution of precursors (SSP). Then, the SSP was spray-dried with temperature of 165 °C to form well dispersion of multimetallic precursors nanoparticles (MPNPs) on GO. Subsequently, as-spray dried precursors on GO were reduced in H₂ atmosphere with moderate heating rate (3 °C/min), thermal decomposition temperature (300−850 °C), duration time (30 min) and low cooling rate (5−10 °C/min), as shown in Figure S5. Pt-based HEA-NPs on reduced graphene oxide (rGO) were obtained. The detailed illustration of synthetic

process of HEA-NPs is shown in Figure 1a and Figure S6. Our method avoided extremely rapid heating and cooling rate, and it made the reaction process easier to accurately controlling. Furthermore, we successfully prepared Pt-based HEA-NPs loaded on different supports, such as carbon nanofibers (CNFs), multiwalled carbon nanotubes (MWCNTs), and super conductive carbon blacks (SCCBs), which proved expandability of SD-TDR technique. Therefore, this facile, low-cost and large-scale SD-TDR method for synthesizing a series of Pt-based HEA-NPs could facilitate a possibility development and application of Pt-based HEA-NPs.

RESULTS AND DISCUSSION

In this experiment, two main procedures, spray drying and thermal decomposition reduction, were used to synthesize HEA-NPs. The Pt-based HEA-NPs with ten immiscible elements (Pt, Ru, Ir, Pd, Rh, Fe, Cu, Ni, Co, W) were synthesized via the SD-TDR method, and the maximum mixing entropy got to be 2.3R (Figure S7). It should be pointed out that the size of HEA-NPs with a low thermal treatment temperature (Figures S8−S11) was too small to
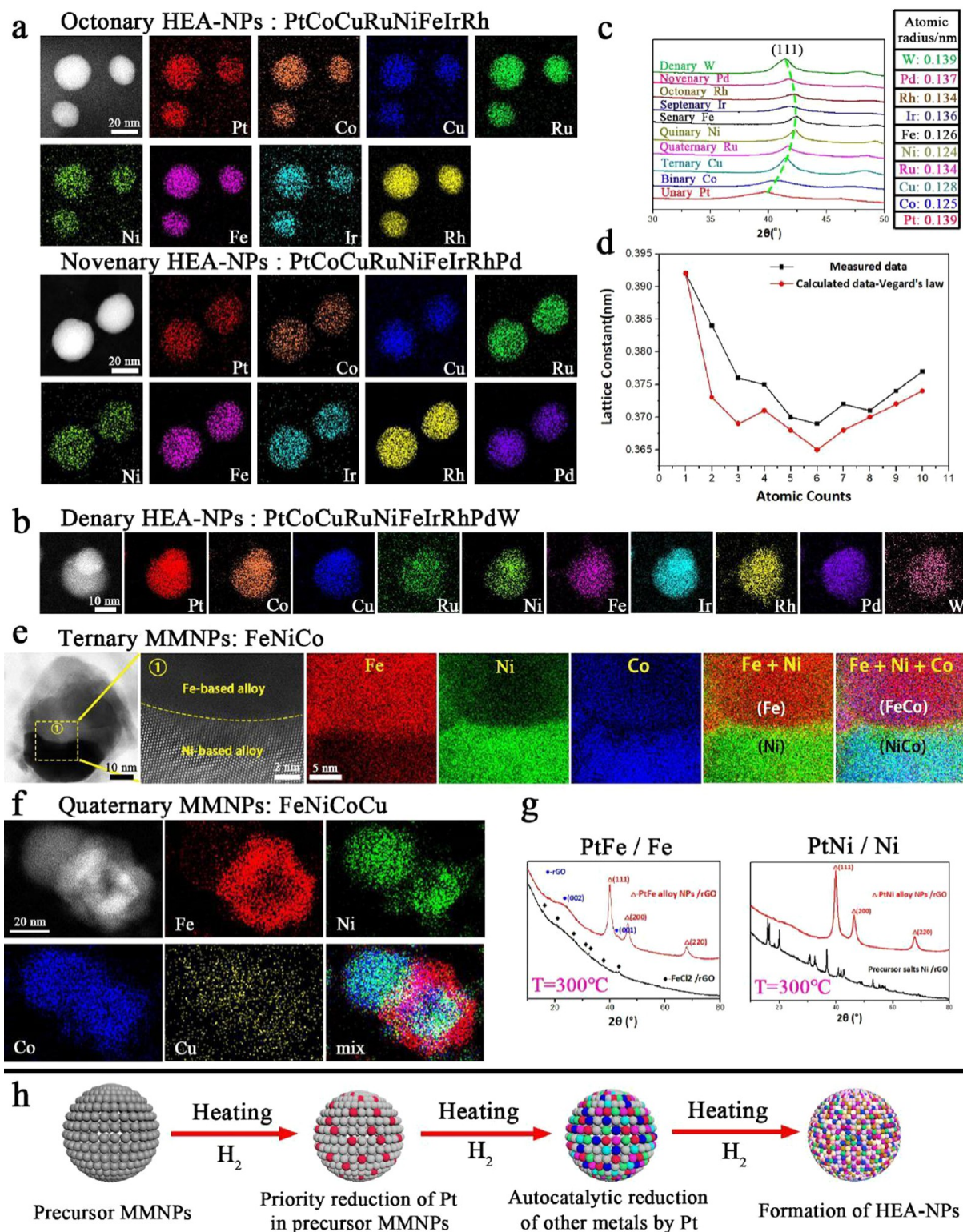
Figure 3. Elemental maps of HEA-NPs, phase structure of MMNPs (1−10 elements), and microstructure characterization of MMNPs without Pt elements. (a) HAADF-STEM images and STEM-EDS elemental maps of octonary PtCoCuRuNiFeIrRh and novenary PtCoCuRuNiFeIrRhPd HEA-NPs obtained at 850 °C. (b) HAADF-STEM images and STEM-EDS elemental maps of denary PtCoCuRuNiFeIrRhPdW HEA-NPs obtained at 850 °C. (c) XRD peak position deviation trend of (111) plane from unary nanoparticles to denary HEA-NPs. (d) Line symbol of lattice constant from unary nanoparticles to denary HEA-NPs; measured data (black line) and calculated data by Vegard's law (red line). (e) ABF, HAADF-STEM images, and STEM-EDS elemental maps of ternary FeNiCo MMNPs with phase separation obtained at 500 °C. (f) HAADF-STEM image and STEM-EDS elemental maps of quaternary FeNiCoCu MMNPs with phase separation obtained at 500 °C. (g) XRD pattern for Fe, Ni, PtFe, and PtNi nanoparticles obtained under 300 °C. (h) Mechanism illustration of Pt element autocatalysis in formation of HEA-NPs.

obtain clear mapping images in high resolution with energy-dispersive X-ray (EDX) spectroscopy, so the large particle size obtained at 850 °C (Figures S12 and S13) was carried out. Denary HEA-NPs were uniformly dispersed on rGO, and single-phase solid solution with a face centered cubic (fcc) crystalline structure was confirmed through the high-angle annular dark-field scanning transmission electron microscopy (HAADF-STEM) images, fast Fourier transform (FFT) analysis and X-ray diffraction (XRD) patterns (Figure 1b). There is no apparent elemental segregation identified in denary HEA-NPs using scanning transmission electron microscopy energy dispersive X-ray (STEM-EDS) elemental maps (Figure 1c).

In the SD process, preparing precursor nanoparticles with evenly mixed elements is the most important step in the preparation of Pt-based HEA-NPs. We simulated the temperature field in the drying chamber, as shown in Figure 1d. The velocity of fogdrops in the center of the drying chamber was also simulated (Figure 1e), which was calculated according to following eq 1:

$$V = V_1 + V_2 = Q_1/S_1 + Q_2/S_2 \qquad (1)$$

where V, V_1, and V_2 are the velocities of fogdrops, the high-pressure gas (HPG) and hot air respectively, Q_1 and Q_2 are the fluxes of HPG and hot air, respectively, and S_1 and S_2 are the sectional areas of the HPG and drying chamber, respectively. The temperature curve in the center of the drying chamber measured under working conditions is presented in Figure 1f. According to the velocity curve of fogdrops, the V (>58 m/s) was very fast under a distance less than 0.01 m; as a result, it took extremely little time (less than 0.000 17s) to cover this distance (0.01 m). Therefore, the heating rate could exceed 104 °C/s when the droplet just emerged from the nozzle. The whole drying chamber was segmented, and the time was calculated. It took less than 0.6 s for the droplets to dry completely. Hereby, the rapid heating rate and instant drying ensured the rapid and uniform precipitation of elements without segregation or local element aggregation. In addition, the dispersion of MPNPs is the key to the formation of nanoparticles. The plentiful oxygen-containing groups (epoxide, hydroxyl, etc.) of GO (Figure S4a) increased the hydrophilicity of substrate, ensuring that GO and the precursor solution did not separate from each other. In the evaporative precursor solution process, many hydrogen bonds were formed between precursor solution and oxygen-containing groups, which provided the guidance of an interaction force to anchor the precursor solution on GO, which involved more oxygen-containing groups, as shown in Figure 2a and Figure S14.

The scanning electron microscope (SEM) images, transmission electron microscopy (TEM) images, and STEM-EDS maps of precursor-loaded GO showed that no obvious agglomeration of nanoparticles or aggregation/segregation of elements were observed in Figures S15−S17, indicating that MPNPs were uniformally distributed across the GO. After the TDR process (500 °C), the micromorphology from unary to denary nanoparticles confirmed the uniform distribution of nanoparticles without aggregation on rGO (Figures S8−S11). The particle size was less than 10 nm. When the reduction temperature was 850 °C, the nanoparticles size grew obviously (Figures S12 and S13). Even so, there was still no significant agglomeration. The formations of single-phase solid solutions (fcc) without secondary phase or intermetallic compounds were demonstrated by the XRD profiles (Figure S18 and S19).

The STEM-EDS elemental maps containing low entropy nanoalloys of unary (Pt, Co, Ru) (Figure S20), binary (PtCo, PtCu) (Figure S20), ternary (PtCoCu, PtCoNi) (Figure S21), and quaternary (PtCoCuRu, PtCoCuIr) (Figure S22) and HEA-NPs of quinary (PtCoNiCuRu, PtCoNiCuPd, PtCoNiCuRh) (Figure 2b and Figure S23), senary (PtCoNiCuRuFe, PtIrPdRuRhCu, PtCoCuRuNiRh) (Figure 2c and Figures S23−S25), septenary (PtIrCoCuNiRuFe) (Figure 2d and Figure S24), octonary (PtCoCuRuNiFeIrRh) (Figure 3a and Figures S25−S27), novenary (PtCoCuRuNiFeIrRhPd) (Figure 3a and Figure S27), and denary (PtCoCuRuNiFeIrRhPdW) (Figure 3b and Figure S28) presented homogeneous element distribution in nanoparticles without obvious agglomeration or segregation between elements, demonstrating that the immiscible elements were alloyed evenly to form solid-solution alloys. We confirmed the presence of the involving elements by STEM-EDS spectra (Figures S29−S32), and the stability of microcosmic and macroscopic compositions (in good agreement with original design of alloy component) was proven by STEM-EDS spectra (Figure S33) and inductively coupled plasma mass spectroscopy (ICP-MS) (Table S3), respectively. Additionally, fully reduced MPNPs (no chlorine content) and the bonding state of metals were confirmed by X-ray photoelectron spectroscopy (XPS) (Figures S34−S45). Therefore, by the SD-TDR method, single-phase solid solutions from unary nanoparticles to denary HEA-NPs were achieved.

The detailed XRD patterns of unary nanoparticles to denary HEA-NPs were analyzed to study the formation law of single-phase solid solution (Figures S18 and S19). The offset of peak (111) location was positively correlated with the radius of alloyed elements (Figure 3c). The deviation trend of (111) plane agreed with the crystalline theory. Furthermore, Vegard's law means that the lattice constant of solid solution composed of the same crystal structure was an intermediate value of the lattice constant of elements and a linear relation with the concentrations of the constituent elements, which was used to estimate theoretical lattice constant.[28] The lattice constant of Vegard's law for MMNPs can be calculated according to following eq 2:

$$a_v = x_1a_1 + x_2a_2 + ... + x_na_n = \sum_{i=1}^{n} x_ia_i \qquad (2)$$

where a_v is the lattice constant of MMNPs, x_i is the mole fraction of the ith element, a_i is the lattice constant of the ith element, and n is the number of elements involved. The line symbols of lattice constant of real data (black line), compared with calculated data by Vegard's law, has the similar tendency (Figure 3d). This determined that as-prepared unary nanoparticles to denary HEA-NPs formed theoretical single-phase solid solution, even though the 10 elements with different lattice constants (Table S1) were immiscible.

We employed HEA-NPs with Pt element containing quaternary (PtCoCuRu), senary (PtCoCuRuNiRh), octonary (PtCoCuRuNiFeIrRh), and denary (PtCoCuRuNiFeIrRhPdW) as examples to investigate the Pt function during the TDR process. The initial single-phase solid solution (fcc) started to form at 150 °C (Figure S47a). The Cl 2p XPS spectra indicated the complete decomposition of MPNPs at 300 °C because of disappearing of Cl 2p XPS peaks (Figures S48 and S49). It confirmed that HEA-NPs containing Pt element can be synthesized at a low thermal decomposition
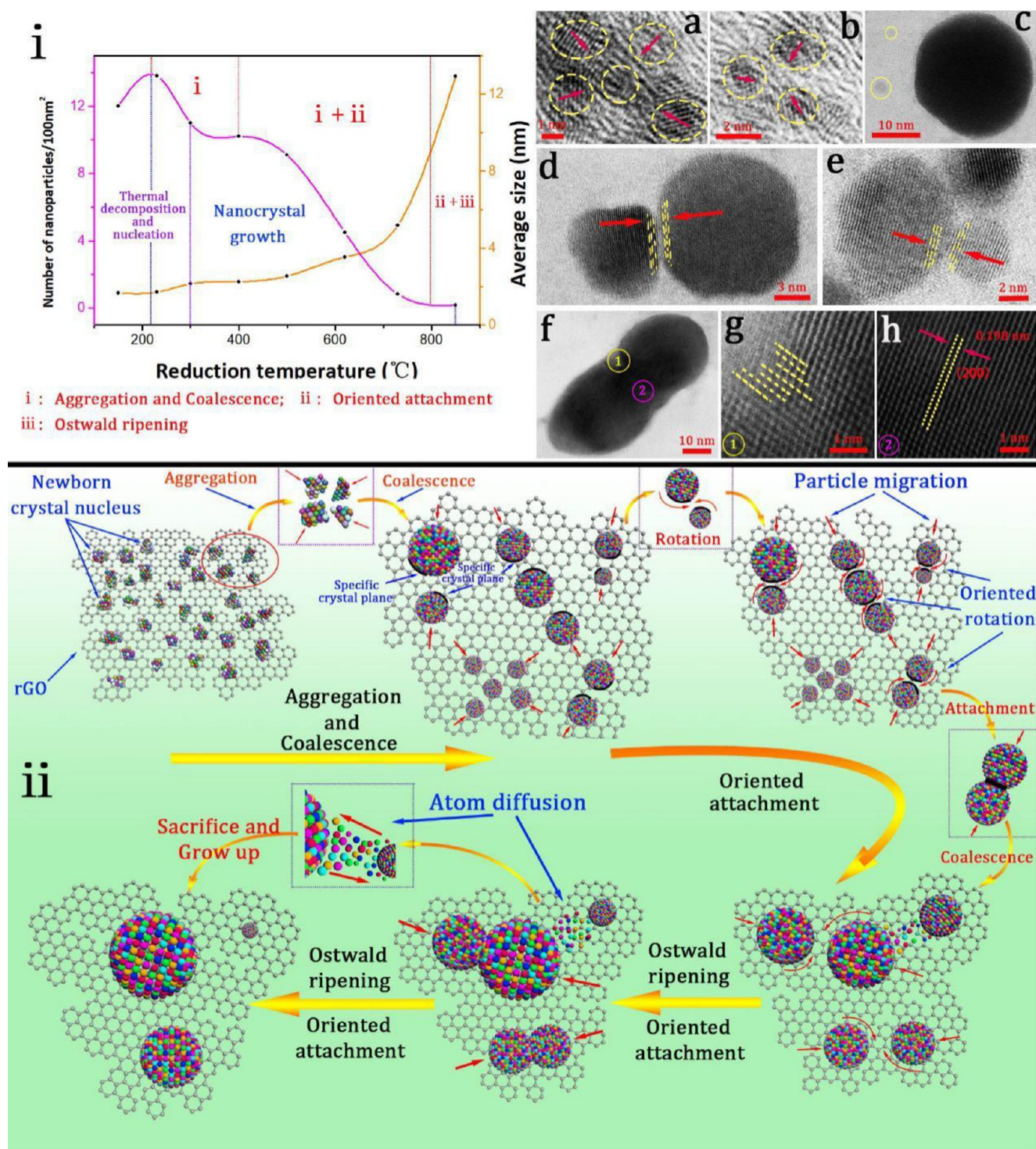
Figure 4. Nanoparticle growth mechanism for the TDR process. (i) The trend of number of nanoparticles per 100 nm² and average size with reduction temperature; it divides the growth of Pt-based HEA-NPs into three regions according to the thermal decomposition temperature: Z-i(AC); Z-i+ii(AC and OA); and Z-ii+iii(OA+OR) (i, Aggregation and Coalescence; ii, Oriented Attachment; iii, Ostwald Ripening). (ii) Schematic representation of growth mechanism of Pt-based HEA-NPs in thermal decomposition reduction process. (a−e) TEM and ABF-STEM images of Pt-based HEA-NPs synthesized at different reduction temperatures: (a) 400 °C; (b) 500 °C; (c) 850 °C; (d) 620 °C; and (e) 730 °C. (f−h) ABF-STEM images of the merging of two nanoparticles obtained at 800 °C (the edges of the two nanoparticles are merging, and it is growing in the same lattice direction).

temperature (300 °C), even though these elements had variant reduction temperature and reduction potentials versus the standard hydrogen electrode (Table S4). However, MMNPs without Pt, such as CoNiFe and CoCuNiFe nanoparticles prepared by SD-TDR, exhibited phase separation, segregation of elements, uncontrollable micromorphology, and high thermal decomposition temperature (more than 400 °C) via XRD patterns, STEM-EDS elemental maps, STEM, XPS, annular bright field (ABF), and HAADF-STEM images (Figures 3e,f and Figures S50−S54). Furthermore, the single
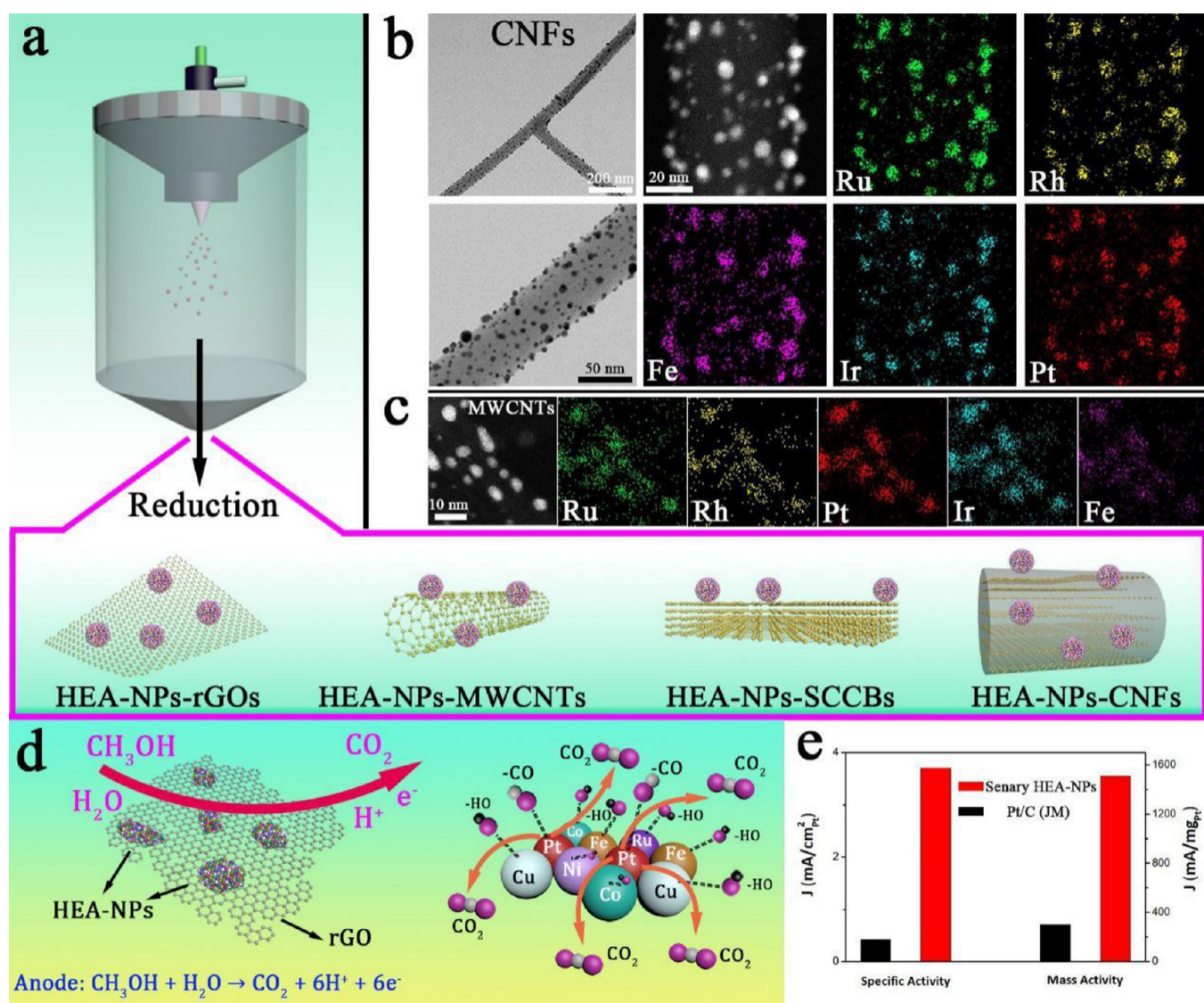
Figure 5. Extensibility of SD-TDR method and performance of electrocatalytic oxidation of methanol using senary HEA-NPs (PtCoCuRuNiFe). (a) Schematic representation of Pt-based HEA-NPs on rGOs, MWCNTs, SCCBs, and CNFs. (b) ABF, HAADF-STEM images, and STEM-EDS elemental maps of quinary PtRuFeIrRh loaded onto CNFs obtained at 500 °C. (c) HAADF-STEM image and STEM-EDS elemental maps of quinary PtRuFeIrRh loaded onto MWCNTs obtained at 500 °C. (d) Detailed schematic diagram for the conversion of CH_3OH to CO_2 on the surface of PtCoCuRuNiFe HEA-NPs. (e) Bar graph illustrating the current density of specific activity (left) and mass activity (right) at peak potential; the CV profiles of senary PtCoCuRuNiFe HEA-NPs and Pt/C (JM) for MOR tested in an aqueous solution of 0.5 M H_2SO_4 and 0.5 M CH_3OH with a scan rate of 50 mV/s.

metal nanoparticles (Pt, Ni, Fe, Cu, Co, and W) and Pt-based bimetallic nanoparticles (PtNi, PtFe, PtCu, PtCo, and PtW) were prepared for studying the role of Pt. The XRD patterns indicated that Pt had the lowest reduction temperature because of the appearance of an initial fcc crystal structure under 150 °C, but other metal precursors (Ni, Fe, Co, and W) cannot be reduced even at 300 °C, as shown in Figure 3g and Figures S55−S58. However, when the Pt element was added to other metals such as Ni, Fe, Cu, Co, and W precursors to form Pt-based precursors, the PtNi, PtFe, PtCu, PtCo, and PtW alloy nanoparticles (fcc crystal structure) without precursor salt phase or other metallic phase can be obtained under 300 °C, as presented in Figure 3g and Figures S56 and S57. Therefore, it declared that the addition of Pt element can decrease the reduction temperature of other transition metals (Ni, Fe, Cu, Co, and W) and form single-phase solid solution (fcc) with

other metals, and although refractory metal W must be reduced at least 700 °C. According to the above study, the mechanism of Pt element catalysis in the formation of HEA-NPs is illustrated in Figure 3h. The noble metal Pt atoms in mixed precursor nanoparticles are preferentially reduced at 150 °C, and then, the reduced Pt atoms catalyze the other elements next to. This chain reaction of Pt autocatalysis becomes more and more as the reaction time until all elements in nanoparticles are fully reduced. After that, the Pt element in precursor MMNPs autocatalyze precursor MMNPs to HEA-NPs with single-phase solid solution (fcc).

In order to precisely control the synthesis process and better understand the growth mechanism of nanoparticles, microstructures transition of senary (PtCoCuRuNiRh) HEA-NPs on large sheets GO was investigated via adjusting thermal decomposition temperature (TDT) from 150 to 850 °C.

The average size of HEA-NPs can be precisely regulated from about 2 to 13 nm through controlling the TDT (Figures S59−S66). Figures S67 and S68 show the line symbol trend of average size of HEA-NPs with reduction temperature and the information on Raman spectra, respectively. The number of nanoparticles per 100 nm^2 of each TEM image, which was obtained by different reduction temperatures (Figure S69), was counted for investigating the relationship between nanoparticles number and TDT (Figure S70). To better understand, we put the average particle size and the number of nanoparticles per 100 nm^2 curves into one picture (Figure 4i), which consisted of two main steps: first, thermal decomposition and nucleation from 150 to 300 °C and, second, nanocrystal growth from about 210 to 850 °C. The growth of Pt-based HEA-NPs, which occurred during TDR, was mainly the gas−solid reaction and the mass transportation between solids, rather than solid−liquid reaction of the wet chemical synthesis. We use three growth patterns to understand growth mechanism, including aggregation and coalescence (AC), oriented attachment (OA), and ostwald ripening (OR),[29−32] as shown in Figure S71.

The growth of Pt-based HEA-NPs was divided into three stages (Figure 4i) according to TDT: Z-i (AC); Z-i+ii (AC and OA); and Z-ii+iii (OA+OR). For Z-I, the newly formed crystal grew mainly via AC due to the high surface energy and the very close distance between clusters at the temperature from 200 to 400 °C (Figure 4a and Figure S72a,b). Although the number of nanoparticles per 100 nm^2 dropped sharply, the average size increased slowly because of less contribution by merging small nanoparticles. For Z-i+ii, the OA growth pattern was dominant by rotating special crystal planes of nanoparticles to grow from 400 to 800 °C (Figure 4d,e and Figure S73a−c), while the AC existed slightly (Figure 4b and Figure S72c,d). The edges of the two nanoparticles were merging (Figure 4f), which grew in the same lattice direction (Figure 4g,h). For Z-ii+iii, the average size increased violently while the number of nanoparticles per 100 nm^2 remained slowly decreasing over 800 °C. It cannot be explained by a single OA growth pattern, because the increasing rate of average particle size did not match the decreasing rate of nanoparticles number per 100 nm^2. Therefore, the OR with a feature of slow decrease in the number of particles combined with the OA (Figure S73d) was employed to explain. Figure 4c presented a large nanoparticle surrounded by small nanoparticles marked in a yellow circle that were about to disappear, confirming that some nanoparticles grow up to abide by OR. By the analysis of Pt-based HEA-NPs growth, we provided a schematic representation of Pt-based HEA-NPs growth mechanism (Figure 4ii).

We also investigated the extensibility of the SD-TDR technique. Alternative carriers, such as carbon nanofibers (CNFs), multiwalled carbon nanotubes (MWCNTs), and super conductive carbon blacks (SCCBs), were employed to synthesize Pt-based HEA-NPs, as shown in Figure 5a. Notice that all alternative carries were hydroxylated via acid treatment to improve their hydrophilicity. The Pt-based HEA-NPs (fcc) without phase separation loaded on CNFs, MWCNTs, and SCCBs, respectively, in which the immiscible elements were uniformly mixed and the nanoparticles were evenly dispersed on the carrier surface, were verified by TEM, XRD, and STEM-EDS elemental maps (Figure 5b,c and Figures S74−S80). Moreover, in our plant, we have achieved the mass production of Pt-based HEA-NPs via the upgraded spray drying machine

and tube furnace (Figure S81), confirming that our SD-TDR is scalable.

In addition, the uniformly mixed Pt-based HEA-NPs with a combination of 5−10 immiscible elements (Pt, Ru, Ir, Pd, Rh, Fe, Cu, Ni, Co, W) can offer alternative materials in catalytic applications, because they have the advanced characteristic of high entropy alloys (high entropy effect, sluggish diffusion effect, severe lattice distortion, and cocktail effect) and nano materials (surface effect, small size effect, tunnel effect of macroscopic quantum, and effect of quantum size). In this study, senary Pt-based HEA-NPs were selected to perform methanol oxidation reaction (MOR) as anodic electrocatalysts for direct methanol fuel cells (DMFCs). The DMFCs, as promising alternative energy conversion devices that had more advantages compared with traditional energy drives, had been developed rapidly.[33] So far, Pt-based alloy materials are still the most effective catalysts, while most are binary and ternary alloys because of the limitation of synthesis methods. Due to multiatom synergy, the performance of Pt-based HEA-NPs are probable to higher than that of binary and ternary alloys, which is a very important strategy for DMFCs commercial application. We employed senary PtCoCuRuFeNi HEA-NPs for MOR testing, which aimed to reduce Pt content and improve the electro-catalysis performance.

HAADF-STEM images, STEM images, STEM-EDS elemental maps, and FFT analysis (Figures S82−S84) indicated the formation of evenly mixed PtCoCuRuNiFe HEA-NPs with single-phase solid solution (fcc) on rGO. During the methanol oxidation reaction, other metal atoms with more negative potentials of adsorption hydroxide around Pt atom tended to adsorb −OH to the formation of M-(OH)$_{ads}$, which could accelerate the elimination of adsorbed CO intermediates from Pt to improve the activity and CO toxicity resistance (Figure 5d and Figure S85).[13,34−36] We tested methanol oxidation performance in an aqueous solution of 0.5 M H$_2$SO$_4$ and 0.5 M CH$_3$OH. The CV curves of MOR (Figures S86 and S87) were normalized by the electrochemically active surface area (ECSA) as well as the mass of Pt loading. The PtCoCuRuNiFe HEA-NPs showed high electrocatalytic performance in the peak current density of Pt ECSA (specific current density) and Pt mass (mass current density) (Figure 5e), which was eight times and five times higher than that of commercial catalysts (Pt/C, 20 wt %, Johnson Matthey, JM), respectively. Moreover, the ratio of I_f/I_b (the forward/backward peak current densities) was used to evaluate the tolerance of catalysts toward the poisoning species (especially CO), and a higher I_f/I_b ratio showed good durability and more efficient conversion of CH$_3$OH to CO$_2$. The senary HEA-NPs exhibited a higher I_f/I_b ratio compared with Pt/C (JM) (1.30 vs 0.88), suggesting that it has better performance of methanol molecules oxidation and relatively fewer poisoning species. We also performed the chronoamperometric (CA) measurements to evaluate the stability of catalysts, and the senary HEA-NPs maintained a higher current density than that of Pt/C (JM) during the entire time range (Figure S88). The HAADF-STEM images, FFT pattern, and the STEM-EDS elemental maps of senary HEA-NPs (PtCoCuRuNiFe) after a CA test indicated that the load state, dispersion, micro crystal structure, and element distribution of the catalyst were well-retained, as illustrated in Figure S89. For a deeper understanding of the relationship between composition and catalytic properties, we synthesized the Pt, PtCo, PtCoCu, PtCoCuRu, PtCoCuRuNi, and PtCoCuRuNiFe nanoparticles on rGO by

SD-TDR method for MOR testing. The CV curves of MOR were normalized by the mass of Pt loading (Figure S90), and the mass current densities were in the order of PtCoCuRuNiFe HEA-NPs > PtCoCuRuNi HEA-NPs > PtCoCuRu alloy nanoparticles (alloy-NPs) > PtCoCu alloy NPs > Pt/C (JM) > PtCo alloy NPs > Pt NPs, indicating that the MOR catalytic properties increased with the increase of element types in composition and the PtCoCuRuNiFe HEA-NPs presented the best property. Thus, it demonstrated that HEA-NPs with a low Pt content (Table S5 for the literature comparison) is a kind of advanced catalyst with promising application foreground.

CONCLUSIONS

In summary, the SD-TDR method for synthesizing HEA-NPs has the following advantages: mild synthesis conditions (T_{min} low to 300 °C, moderate heating (3 °C/min) and cooling (5−10 °C/min) rates), controllability, expandability, low cost, and high productivity. A series of Pt-based HEA-NPs with a single-phase solid solution containing noble metal, transition metal, and refractory metal (Pt, Ru, Ir, Pd, Rh, Fe, Cu, Ni, Co, W) were synthesized, and the SD-TDR method avoided extremely rapid heating and cooling rates, which made the reaction process easier to accurately control. The Pt-based HEA-NPs prepared by the SD-TDR method maintained the following features. First, for uniform mixing of immiscible elements, the SSP without any organic additives was spray-dried instantly to avoid segregation or aggregation of elements in the precursor nanoparticles, and the existence of Pt metals prevented phase separation and ensured all elements to be reduced simultaneously into a single nanoparticle. Second, for uniform dispersion on carbon substrates, the key oxygen-containing groups provided anchoring sites to facilitate nanoparticle dispersion by the guidance of an interaction force (the hydrogen bonds). Third, for controllable nanoparticles size, the study of growth mechanism and thermal decomposition enabled targetedly sized nanoparticles. Finally, for a high entropy level, Pt-based HEA-NPs with evenly mixed elements guaranteed maximized configurational mixing. The enormous kinds of single-phase solid solution from binary nanoparticles to denary Pt-based HEA-NPs with different components and proportions can be synthesized by the SD-TDR method, which is expected to lay the foundation for the selection of Pt-based HEA-NPs and large-scale preparation.

EXPERIMENTAL SECTIOINS

Materials. Multiple layers of graphene oxide (GO) as carriers were homemade. Precious metal compounds, $(NH_4)_2PtCl_6$, $RuCl_3 \cdot 3H_2O$, $(NH_4)_2IrCl_6$, $RhCl_3 \cdot 3H_2O$, and $PdCl_2$ were purchased from Sino Platinum Metals (Yimen) Co. LTD. (Yimen, Yunnan, P. R. China). Other compounds, $CuCl_2 \cdot 2H_2O$, $FeCl_3 \cdot 6H_2O$, $NiCl_2 \cdot 6H_2O$, $CoCl_2 \cdot 6H_2O$, $(NH_4)_{10}[H_2W_{12}O_{42}] \cdot 4H_2O$, HCl (37.5 wt %), H_2SO_4 (98%), methanol (AR.), 2-propanol (AR.), and ethanol (AR.) were purchased from Sigma (St. Louis, MO). High-purity hydrogen (H_2) was obtained from Pengyida Co. LTD. (Kunming, Yunnan, China). The deionized water was used as the solvent, and all reagents and solvents were used as received without further purification. In addition, carbon nanofibers (CNFs), multiwalled carbon nanotubes (MWCNTs), and super conductive carbon blacks (SCCBs) as alternative carriers were purchased from Suzhou Carbon-Rich Graphene Technology Co., LTD. (Suzhou, Jiangsu, China).

Preparation of Steady-State Solution of the Precursors (SSP). A certain amount of precursor salts ($(NH_4)_2PtCl_6$, $RuCl_3 \cdot 3H_2O$, $(NH_4)_2IrCl_6$, $RhCl_3 \cdot 3H_2O$, $(NH_4)_{10}[H_2W_{12}O_{42}] \cdot 4H_2O$, $PdCl_2$, $CuCl_2 \cdot 2H_2O$, $FeCl_3 \cdot 6H_2O$, $NiCl_2 \cdot 6H_2O$, $CoCl_2 \cdot 6H_2O$) were weighed according to the equal atomic ratio, which were added to

deionized water (0.001 mol/L for each element). The precursors solution was heated to 60 °C and ultrasonic stirred for 2 h. When the solution was free of any precipitations, GO was added with ultrasonic stirring for 1 h. A steady-state solution of the precursors (SSP) was obtained.

Spray Drying (SD) Process of SSP. The solution of precursors (500 mL) with a concentration of 0.001 mol/L for each element, composed of 10 kinds of metal elements (Pt, Ru, Ir, Rh, W, Pd, Cu, Fe, Ni, Co) and the carbon supports, was spray-dried by the home-designed spray dryer. In this Experimental Section, the inlet temperature, feed rate, HPG flow rate, and drying gas flow rate were 165 °C, 200 mL/h, 1.3 L/s, and 35 m^3/h, respectively. When the equipment worked steadily, the SSP was introduced into the equipment to be atomized. After 2.5 h, precursors nanoparticles loaded onto GO were collected.

Thermal Decomposition and Alloying Process of Precursors Nanoparticles. A tube furnace from Hefei Kejing material technology Co. LTD (OTF-1200X, Hefei, China) was utilized to alloy 1−10 dissimilar metallic elements into a single nanoparticle. A diagram of thermal decomposition is shown in Figure S5. The precursors nanoparticles loaded onto GO were located in a tube furnace. Then, the tube furnace was treated by a vacuum. Subsequently, precursor nanoparticles and GO were reduced to multimetallic nanoparticles (MMNPs) and reduced graphene oxide (rGO) in an H_2 atmosphere, respectively, with a moderate heating rate of 3 °C/min, a low thermal decomposition temperature of 300−850 °C, a duration time of 30 min, and a cooling rate of 5−10 °C/min. In the process of thermal decomposition, HCl, NH_3, and H_2O were released. Multimetallic precursors nanoparticles (MPNPs) were decomposed to MMNPs (including Pt, Ru, Ir, Rh, W, Pd, Cu, Fe, Ni, Co), which were Pt-based high-entropy-alloy nanoparticles (HEA-NPs).

$$MPNPs \overset{H_2}{\underset{\Delta}{\rightarrow}} H_2O + HCl + NH_3 + MMNPs$$

$$GO \overset{H_2}{\underset{\Delta}{\rightarrow}} rGO + H_2O$$
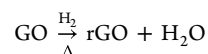
Catalytic Methanol Oxidation Tests. An electrochemical analyzer instrument from Shanghai Chenhua Instrument Co. LTD (Chi760e, Shanghai, China) and a standard three-electrode electrochemical cell consisting of a Pt mesh, Ag/AgCl electrode, and glass carbon electrode from Tianjin Aida hengsheng technology Co. LTD (Tianjin, China) were used for performing catalytic methanol oxidation reaction. Typically, 5 mg of the prepared PtCoNiCuFeRu HEA-NPs (30 wt % and equal atomic ratio) loaded on rGO was dispersed in 2.5 mL of mixed solvent containing deionized water, 2-propanol, and 5% Nafion (Aldrich Chemistry) (volume ratio is 4:1:0.025). Then, it was sonicated for 15 min to prepare the catalyst ink. Ten microliters of the catalyst ink was deposited onto a precleaned GCE as the working electrode, which was dried at room temperature. The glassy carbon diameter of GCE was 5 mm, and the geometric area was 0.196 cm^2. Typical cyclic voltammetry (CV) and chronoamperometry (CA) were carried out, and Ag/AgCl electrode was used as the reference electrode and a 1 × 1 cm^2 Pt mesh was used as the counter electrode.

Cyclic voltammetry (CV) curves were started in a deoxygenated 0.5 M H_2SO_4 solution in the voltage range from −0.22 to +0.98 V (vs Ag/AgCl) with a scan rate of 150 mV/s until the CV curves became stable. After that, the CV curves were achieved at a scan rate of 50 mV/s. The catalytic activities toward methanol were recorded in deoxygenated 0.5 M H_2SO_4 containing 0.5 M CH_3OH in the voltage range from −0.22 to +0.98 V (vs Ag/AgCl) at a scan rate of 50 mV/s. The stable CV curves were obtained after about 40 cycles scanning. The current stability was measured using the CA technique under identical conditions as the electrooxidation of methanol at a potential of 0.65 V (vs Ag/AgCl) for 2000 s.

Characterization. Scanning electron microscopy (SEM) images of precursor-loaded supports were taken with a Hitachi S-8030 field-emission scanning electron microscope at an acceleration voltage of 5

kV and a current of 20 μA. The microstructures of samples were observed using a transmission electron microscope (TEM). Atomic-scale characterization of the HEA-NPs was conducted on a JEM Grand ARM 300 (cold FEG) operated at an accelerating voltage of 300 kV with both a probe and image corrector. For the STEM (scanning transmission electron microscopy) images, the convergence semiangle of the probe was set as ≈24.5 mrad, and the collection angle of the annular bright field (ABF) and high-angle annular dark field (HAADF) detectors were 11−22 and 54−220 mrad, respectively. The energy dispersive X-ray (EDS) spectra were recorded using a dual-EDS system (JED-2300T) incorporating two large windowless SDD detectors with a total solid angle of 2.2 sr. X-ray photoelectron spectroscopy (XPS) results were detected on an Axis Ultra DLD photoelectron spectrometer using Al Kα (1486.6 eV) radiation. X-ray diffraction (XRD) patterns were obtained with a Bruker D8 ADVANCE (Bruker AXS, WI, USA) using Cu Kα radiation with a scan rate of 3°/min. Raman spectra were performed at room temperature using a laser raman spectrometer (LabRAM HR Evolution) with a 514 nm excitation wavelength. The metal contents in the HEA-NPs were measured by inductively coupled plasma mass spectroscopy (300D ICP-MS).

ASSOCIATED CONTENT

ⓈⒾ Supporting Information

The Supporting Information is available free of charge at https://pubs.acs.org/doi/10.1021/acsnano.2c03818.

> Dicussions of selection of precursor salts and carbon carriers, structural characterization of GO and rGO, synthetic process of Pt-based HEA-NPs, configurational entropy of component, uniform precipitation of elements in nanoparticles by SD, dispersing multi-metallic precursor nanoparticles on GO by SD, micro-structure of multimetallic precursor nanoparticles, STEM-EDS elemental maps of multimetallic precursor nanoparticles, microstructures of Pt-based HEA-NPs, XRD analysis of Pt-based HEA-NPs, STEM-EDS elemental maps and STEM-EDS spectrum of Pt-based HEA-NPs, XPS analysis of HEA-NPs, ICP-MS analysis for Pt-based HEA-NPs composition, Pt-based HEA-NPs anchored firmly on the surface of rGO, thermal decomposition temperature study of Pt-based HEA-NPs, role of Pt metal in Pt-based HEA-NPs, Pt function for formation of Pt-based HEA-NPs on rGO, Pt-based HEA-NPs growth mechanism, universality for preparing MMNPs containing Pt-based HEA-NPs by SD-TDR method, preliminary study of performance for Pt-based HEA-NPs, potential application of Pt-based HEA-NPs loaded different substrates, and feasibility analysis of large yield production of Pt-based HEA-NPs, figures of schematic illustration of the home-designed spray dryer, elemental precursors solutions used to prepare Pt-based HEA-NPs on rGO, TEM image and Raman spectrum of GO, XPS spectra, XRD patterns, schematic illustration of thermal decomposition reduction in tube furnace, illustration of synthetic process of Pt-based HEA-NPs, relationship between mixing entropy and MMNPs, TEM images, schematic of dispersion of polymetallic precursor salts, microstructure of eight elemental precursors loaded on GO, STEM-EDS elemental maps of eight elemental precursors loaded on GO, STEM-EDS elemental maps, STEM-EDS spectra, STEM images, size distribution, line symbol of trend of average size with reduction temperature, Raman spectra, schematic representation of trend of number of nanoparticles, schematic representation of three growth mechanism of

> nanoparticles under different thermal decomposition conditions, schematic illustration of the large yield production of Pt-based HEA-NPs using SD-TDR method, FFT anaysis, schematic diagrams and reaction equations of the MOR process using senary (PtCoCuR-uNiFe) HEA-NPs, and CV curves, and tables of atomic radius, lattice constant of single element, real lattice constant of MMNPs, and lattice constant of Vegard's law, miscibility of two elements with a 1:1 ratio, ICP-MS composition of HEA-NPs, physical and chemical properties of metals and precursor salts, and comparative study of the MOR activity with recently reported literature (PDF)

AUTHOR INFORMATION

Corresponding Authors

Panchao Zhao − *Northwest Institute for Non-ferrous Metal Research, Xi'an 710016, People's Republic of China;* ⓞ orcid.org/0000-0003-0729-0111; Email: zhaopc.qing@qq.com

Qigao Cao − *Northwest Institute for Non-ferrous Metal Research, Xi'an 710016, People's Republic of China;* Email: caoqigao@c-nin.com

Wei Yi − *Kunming Institute of Precious Metals, Kunming 650221, People's Republic of China; School of Materials Science and Engineering, Nanchang University, Nanchang 330031, People's Republic of China;* Email: yiwei@ncu.edu.cn

Xiaodong Hao − *Materials Institute of Atomic and Molecular Science, Shaanxi University of Science and Technology, Xi'an 710021, People's Republic of China;* ⓞ orcid.org/0000-0003-2465-9494; Email: hao.xiaodong@sust.edu.cn

Zhiwei Shan − *State Key Laboratory for Mechanical Behavior of Materials, Xi'an Jiaotong University, Xi'an 710049, People's Republic of China;* Email: zwshan@xjtu.edu.cn

Jialin Chen − *Kunming Institute of Precious Metals, Kunming 650221, People's Republic of China;* Email: cjl@ipm.com.cn

Authors

Jigang Li − *Kunming Institute of Precious Metals, Kunming 650221, People's Republic of China*

Bosheng Zhang − *Northwest Institute for Non-ferrous Metal Research, Xi'an 710016, People's Republic of China;* ⓞ orcid.org/0000-0003-2450-4492

Long Huang − *Kunming Institute of Precious Metals, Kunming 650221, People's Republic of China*

Yujie Huang − *Northwest Institute for Non-ferrous Metal Research, Xi'an 710016, People's Republic of China*

Yunbo Jiang − *Kunming Institute of Precious Metals, Kunming 650221, People's Republic of China*

Bingshe Xu − *Materials Institute of Atomic and Molecular Science, Shaanxi University of Science and Technology, Xi'an 710021, People's Republic of China*

Complete contact information is available at:
https://pubs.acs.org/10.1021/acsnano.2c03818

Author Contributions

P.Z., Q.C., and W.Y. conceived the idea and designed the present work. P.Z. carried out the experiments. X.H. and B.X. designed and performed the STEM experiments and the data analysis. J.C., Z.S., and Y.H. supervised the project and provided the XRD analysis. J.L. carried out Raman spectrum

REFERENCES

(1) Yao, Y.; Huang, Z.; Xie, P.; Lacey, S. D.; Jacob, R. J.; Xie, H.; Chen, F.; Nie, A.; Pu, T.; Rehwoldt, M.; et al. Carbothermal shock synthesis of high-entropy-alloy nanoparticles. *Science* **2018**, *359* (6383), 1489−1494.

(2) Yao, Y.; Liu, Z.; Xie, P.; Huang, Z.; Li, T.; Morris, D.; Finfrock, Z.; Zhou, J.; Jiao, M.; Gao, J.; et al. Computationally aided, entropy-driven synthesis of highly efficient and durable multi-elemental alloy catalysts. *Sci. Adv.* **2020**, *6* (11), No. eaaz0510.

(3) Gao, S.; Hao, S.; Huang, Z.; Yuan, Y.; Han, S.; Lei, L.; Zhang, X.; Shahbazian-Yassar, R.; Lu, J. Synthesis of high-entropy alloy nanoparticles on supports by the fast moving bed pyrolysis. *Nat. Commun.* **2020**, *11* (1), 1−11.

(4) Liu, M.; Zhang, Z.; Okejiri, F.; Yang, S.; Zhou, S.; Dai, S. Entropy-maximized synthesis of multimetallic nanoparticle catalysts via a ultrasonication-assisted wet chemistry method under ambient conditions. *Advanced Materials Interfaces* **2019**, *6* (7), 1900015.

(5) Qiu, H. J.; Fang, G.; Wen, Y.; Liu, P.; Xie, G.; Liu, X.; Sun, S. Nanoporous high-entropy alloys for highly stable and efficient catalysis. *Journal of Materials Chemistry A* **2019**, *7* (11), 6499−6506.

(6) Qiu, H.; Fang, G.; Gao, J.; Wen, Y.; Sun, S.; et al. Noble metal-free nanoporous high-entropy alloys as high efficient electrocatalysts for oxygen evolution reaction. *ACS Materials Lett.* **2019**, *1* (5), 526−533.

(7) Huang, K.; Zhang, B. W.; Wu, J. S.; Zhang, T. Y.; Peng, D. D.; Cao, X.; Zhang, Z.; Li, Z.; Huang, Y. Z. Exploring the impact of atomic lattice deformation on oxygen evolution reactions based on a sub-5 nm pure face-centred cubic high-entropy alloy electrocatalyst. *J. Mater. Chem. A* **2020**, *8* (24), 11938−11947.

(8) Cui, X. D.; Zhang, B. L.; Zeng, C. Y.; Guo, S. M. Electrocatalytic activity of high-entropy alloys toward oxygen evolution reaction. *MRS Commun.* **2018**, *8* (3), 1230−1235.

(9) Jin, Z.; Lv, J.; Jia, H.; Liu, W.; Li, H.; Chen, Z.; Lin, X.; Xie, G.; Liu, X.; Sun, S.; et al. Nanoporous Al-Ni-Co-Ir-Mo high-entropy alloy for record-high water splitting activity in acidic environments. *Small* **2019**, *15* (47), 1904180.

(10) Nellaiappan, S.; Katiyar, N. K.; Kumar, R.; Parui, A.; Malviya, K. D.; Pradeep, K. G.; Singh, A. K.; Sharma, S.; Tiwary, C. S.; Biswas, K. High-entropy alloys as catalysts for the CO₂ and CO reduction reactions: experimental realization. *ACS Catal.* **2020**, *10* (6), 3658−3663.

(11) Pedersen, J. K.; Batchelor, T. A. A.; Bagger, A.; Rossmeisl, J. High-entropy alloys as catalysts for the CO₂ and CO reduction reactions. *ACS Catal.* **2020**, *10* (3), 2169−2176.

(12) Wu, D.; Kusada, K.; Yamamoto, T.; Toriyama, T.; Matsumura, S.; Kawaguchi, S.; Kubota, Y.; Kitagawa, H. Platinum-group-metal high-entropy-alloy nanoparticles. *J. Am. Chem. Soc.* **2020**, *142* (32), 13833−13838.

(13) Li, H. D.; Han, Y.; Zhao, H.; Qi, W. J.; Zhang, D.; Yu, Y. D.; Cai, W. W.; Li, S. X.; Lai, J. P.; Huang, B. L.; Wang, L. Fast site-to-site electron transfer of high-entropy alloy nanocatalyst driving redox electrocatalysis. *Nat. Commun.* **2020**, *11*, 5437.

(14) Chen, X. T.; Si, C. H.; Gao, Y. L.; Frenzel, J.; Sun, J.; Eggeler, G.; Zhang, Z. Multi-component nanoporous platinum ruthenium copper osmium iridium alloy with enhanced electrocatalytic activity towards methanol oxidation and oxygen reduction. *J. Power Sources* **2015**, *273*, 324−332.

(15) Batchelor, T. A.; Pedersen, J. K.; Winther, S. H.; Castelli, I. E.; Jacobsen, K. W.; Rossmeisl, J. High-entropy alloys as a discovery platform for electrocatalysis. *Joule.* **2019**, *3* (3), 834−845.

(16) Qiao, H. Y.; Saray, M. T.; Wang, X. Z.; Xu, S. M.; Chen, G.; Huang, Z. N.; Chen, C. J.; Zhong, G.; Dong, Q.; Hong, M.; Xie, H.; Shahbazian-Yassar, R.; Hu, L. B. Scalable synthesis of high entropy alloy nanoparticles by microwave heating. *ACS Nano* **2021**, *15* (9), 14928−14937.

(17) Buck, M. R.; Bondi, J. F.; Schaak, R. E. A total-synthesis framework for the construction of high-order colloidal hybrid nanoparticles. *Nat. Chem.* **2012**, *4* (1), 37−44.

(18) Chen, P.-C.; Liu, X.; Hedrick, J. L.; Xie, Z.; Wang, S.; Lin, Q.-Y.; Hersam, M. C.; Dravid, V. P.; Mirkin, C. A. Polyelemental nanoparticle libraries. *Science* **2016**, *352* (6293), 1565−1569.

(19) Sankar, M.; Dimitratos, N.; Miedziak, P. J.; Wells, P. P.; Kiely, C. J.; Hutchings, G. J. Designing bimetallic catalysts for a green and sustainable future. *Chem. Soc. Rev.* **2012**, *41* (24), 8099−8139.

(20) Wu, D.; Kusada, K.; Yamamoto, T.; Toriyama, T.; Matsumura, S.; Kawaguchi, S.; Kubota, Y.; Kitagawa, H. Platinum-group-metal high-entropy-alloy nanoparticles. *J. Am. Chem. Soc.* **2020**, *142* (32), 13833−13838.

(21) Broge, N. L.; Bondesgaard, M.; Søndergaard-Pedersen, F.; Roelsgaard, M.; Iversen, B. B. Autocatalytic Formation of High-Entropy Alloy Nanoparticles. *Angew. Chem.* **2020**, *132* (49), 22104−22108.

(22) Nandiyanto, A. B. D.; Okuyama, K. Progress in developing spray-drying methods for the production of controlled morphology particles: From the nanometer to submicrometer size ranges. *Adv. Powder Technol.* **2011**, *22* (1), 1−19.

(23) Carné-Sánchez, A.; Imaz, I.; Cano-Sarabia, M.; Maspoch, D. A spray-drying strategy for synthesis of nanoscale metal-organic frameworks and their assembly into hollow superstructures. *Nat. Chem.* **2013**, *5* (3), 203−211.

(24) Boissiere, C.; Grosso, D.; Chaumonnot, A.; Nicole, L.; Sanchez, C. Aerosol route to functional nanostructured inorganic and hybrid porous materials. *Adv. Mater.* **2011**, *23* (5), 599−623.

(25) Chui, S. S.-Y.; Lo, S. M.-F.; Charmant, J. P.; Orpen, A. G.; Williams, I. D. A chemically functionalizable nanoporous material [Cu₃(TMA)₂ (H₂O)₃]ₙ. *Science* **1999**, *283* (5405), 1148−1150.

(26) Zhu, Y.; Choi, S. H.; Fan, X.; Shin, J.; Ma, Z.; Zachariah, M. R.; Choi, J. W.; Wang, C. Recent progress on spray pyrolysis for high performance electrode materials in lithium and sodium rechargeable batteries. *Adv. Energy Mater.* **2017**, *7* (7), 1601578.

(27) Balgis, R.; Anilkumar, G. M.; Sago, S.; Ogi, T.; Okuyama, K. Nanostructured design of electrocatalyst support materials for high-performance PEM fuel cell application. *J. Power Sources* **2012**, *203*, 26−33.

(28) Denton, A. R.; Ashcroft, N. W. Vegard's law. *Phys. Rev. A* **1991**, *43* (6), 3161.

(29) Liao, H.-G.; Cui, L.; Whitelam, S.; Zheng, H. Real-time imaging of Pt₃Fe nanorod growth in solution. *Science* **2012**, *336* (6084), 1011−1014.

(30) Tao, F. F.; Salmeron, M. In situ studies of chemistry and structure of materials in reactive environments. *Science* **2011**, *331* (6014), 171−174.

(31) Wang, F.; Richards, V. N.; Shields, S. P.; Buhro, W. E. Kinetics and mechanisms of aggregative nanocrystal growth. *Chem. Mater.* **2014**, *26* (1), 5−21.

(32) Zheng, H.; Smith, R. K.; Jun, Y.-w.; Kisielowski, C.; Dahmen, U.; Alivisatos, A. P. Observation of single colloidal platinum nanocrystal growth trajectories. *Science* **2009**, *324* (5932), 1309−1312.

(33) Gottesfeld, S.; Dekel, D. R.; Page, M.; Bae, C.; Yan, Y.; Zelenay, P.; Kim, Y. S. Anion exchange membrane fuel cells: Current status and remaining challenges. *J. Power Sources* **2018**, *375*, 170−184.

(34) Chen, A.; Ostrom, C. Palladium-based nanomaterials: synthesis and electrochemical applications. *Chem. Rev.* **2015**, *115* (21), 11999−12044.

(35) Xia, B. Y.; Wu, H. B.; Wang, X.; Lou, X. W. One-pot synthesis of cubic PtCu$_3$ nanocages with enhanced electrocatalytic activity for the methanol oxidation reaction. *J. Am. Chem. Soc.* **2012**, *134* (34), 13934−13937.

(36) Ali, A.; Shen, P. K. Recent advances in graphene-based platinum and palladium electrocatalysts for the methanol oxidation reaction. *J. Mater. Chem. A* **2019**, *7* (39), 22189−22217.